

The evolution of host mass and black hole mass in QSOs from the 2dF QSO Redshift Survey

S. Fine^{1,2*}, S. M. Croom², L. Miller³, A. Babic³, D. Moore², B. Brewer²
 R. G. Sharp², B. J. Boyle⁴, T. Shanks⁵, R. J. Smith⁶, P. J. Outram⁵, N. S. Loaring⁷

¹*School of Physics, University of Sydney, NSW 2006, Australia*

²*Anglo-Australian Observatory, PO Box 296, Epping, NSW 1710, Australia.*

³*Department of Physics, Oxford University, Keble Road, Oxford, OX1 3RH, UK.*

⁴*Australia Telescope National Facility, PO Box 76, Epping, NSW 1710, Australia.*

⁵*Physics Department, University of Durham, South Road, Durham, DH1 3LE, UK.*

⁶*Astrophysics Research Institute, Liverpool John Moores University, Twelve Quays House, Egerton Wharf, Birkenhead, CH41 1LD, UK*

⁷*Mullard Space Science Laboratory, Holmbury St. Mary, Dorking, Surrey, RH5 6NT, UK*

30 October 2018

ABSTRACT

We investigate the relation between the mass of super-massive black holes (M_{BH}) in QSOs and the mass of the dark matter halos hosting them (M_{DH}). We measure the widths of broad emission lines (Mg II $\lambda 2798$, C IV $\lambda 1549$) from QSO composite spectra as a function of redshift. These widths are then used to determine virial black hole mass estimates.

We compare our virial black hole mass estimates to dark matter halo masses for QSO hosts derived by Croom et al. (2005) based on measurements of QSO clustering. This enables us to trace the $M_{\text{BH}} - M_{\text{DH}}$ relation over the redshift range $z = 0.5$ to 2.5. We calculate the mean zero-point of the $M_{\text{BH}} - M_{\text{DH}}$ relation to be $M_{\text{BH}} = 10^{8.4 \pm 0.2} M_{\odot}$ for an $M_{\text{DH}} = 10^{12.5} M_{\odot}$. These data are then compared with several models connecting M_{BH} and M_{DH} as well as recent hydrodynamical simulations of galaxy evolution. We note that the flux limited nature of QSO samples can cause a Malmquist-type bias in the measured zero-point of the $M_{\text{BH}} - M_{\text{DH}}$ relation. The magnitude of this bias depends on the scatter in the $M_{\text{BH}} - M_{\text{DH}}$ relation, and we reevaluate the zero-point assuming three published values for this scatter.

We create a subsample of our data defined by a constant magnitude interval around L^* and find $(1+z)^{3.3 \pm 1.3}$ evolution in M_{BH} between $z \sim 0.5$ and 2.5 for typical, L^* QSOs. We also determine the Eddington ratios (L/L_{Edd}) for the same subsample and find no significant evolution: $(1+z)^{-0.4 \pm 1.1}$. Taken at face value, our data suggest that a decrease in active black hole mass since $z \sim 2.5$ is the driving force behind luminosity evolution of typical, L^* , optically selected AGN. However, we note that our data are also consistent with a picture in which reductions in both black hole mass and accretion rate contribute equally to luminosity evolution. In addition we find these evolution results are strongly affected by the virial black hole mass estimators used. Changes to the calibration of these has a significant effect on the evolution results.

Key words: galaxies: clustering – galaxies: evolution – galaxies: haloes – quasars: general – quasars: emission lines – cosmology: observations

1 INTRODUCTION

Over recent years it has become apparent that massive black holes lie at the centre of the majority of local galaxies. In addition, correlations between the mass of these central

black holes (M_{BH}) and host galaxy properties suggests that the evolution of galaxies must be intimately related to the growth of their central black holes. Galaxy properties which display a correlation with M_{BH} include spheroid luminosity (Magorrian et al. 1998), spheroid mass (Kormendy & Richstone 1995; Ferrarese 2002) and stellar velocity dispersion (Ferrarese & Merritt 2000; Gebhardt et al. 2000).

* sfine@physics.usyd.edu.au

In this paper we investigate the relationship between the mass of QSO black holes and the mass of the dark matter halos that host them. Dark matter halo masses derived from QSO clustering were calculated for QSOs in the 2dF QSO Redshift Survey (2QZ; Croom et al. 2004) by Croom et al. (2005). These were evaluated for QSOs in 10 redshift bins from $z \sim 0.5$ to 2.5. We take the identical sample to that used by Croom et al. (2005) and calculate average virial black hole masses for the QSOs in each redshift bin. This is achieved by constructing a composite spectrum for each redshift bin from all of the QSOs in that bin. The average virial black hole masses are then estimated from the widths of broad emission lines in the composite spectra.

In Section 2 we describe the virial black hole mass estimators used in this paper, section 3 describes our data and analysis including composite making and line width measurement. In Section 4 we briefly review the clustering measurements which are used to derive dark halo host mass. Our results are presented in Section 5 and we present our conclusions in Section 6.

Throughout this paper we assume a flat $(\Omega_m, \Omega_\Lambda) = (0.3, 0.7)$, $H_0 = 70 \text{ km s}^{-1} \text{ Mpc}^{-1}$ cosmology.

2 BLACK HOLE MASS ESTIMATES

At the basis of measuring QSO black hole masses is the virial theorem such that the black hole mass $M_{\text{BH}} \approx rv^2/G$, where v is the velocity dispersion of material gravitationally bound to the black hole at a distance r from it. Direct measurements of r and v have been taken, for relatively nearby systems, in a variety of ways. Most notably reverberation mapping programs have succeeded in accurately measuring M_{BH} for tens of local QSOs (Wandel, Peterson, & Malkan 1999; Kaspi et al. 2000; Peterson et al. 2004). This technique requires careful long-term observations of the variability in QSO spectra and can take years to produce results. Therefore there has been considerable effort put into finding quicker, simpler methods for estimating black hole masses which can be extended to higher redshifts.

One result of reverberation studies of nearby QSOs was the discovery of a strong correlation between the radius of the $\text{H}\beta$ emitting region around AGN, $r_{\text{H}\beta}$, and the continuum luminosity at 5100 Å (Kaspi et al. 2000; Kaspi et al. 2005). $v_{\text{H}\beta}$ can be found by the relation $v_{\text{H}\beta} = f \cdot \text{FWHM}(\text{H}\beta)$ where $\text{FWHM}(\text{H}\beta)$ is the measured full width at half maximum of the $\text{H}\beta$ spectral line, and f is factor of order unity which depends on the geometry of the broad line emitting region around the AGN. Thus, using the width of the $\text{H}\beta$ line and the continuum luminosity at 5100 Å single epoch estimates for M_{BH} can be made (Kaspi et al. 2000; Vestergaard & Peterson 2006).

In higher redshift QSOs the $\text{H}\beta$ line is redshifted out of the optical spectrum. At these higher redshifts UV lines can be used to try and estimate M_{BH} . Unfortunately, while the velocity dispersions, v_{UV} , can readily be measured there is no direct way to measure the size of the of the emitting region r_{UV} . Hence these estimators must be calibrated with $\text{H}\beta$ measurements of the same object. These calibrations have been performed for the Mg II and C IV lines by McLure & Jarvis (2002) and Vestergaard (2002) respectively. The relation for Mg II was then revised for luminous QSOs by

McLure & Dunlop (2004), and the relation for C IV was revised for an updated cosmology by Vestergaard & Peterson (2006). The resulting M_{BH} estimators used throughout this paper are

$$\frac{M_{\text{BH}}}{M_\odot} = 3.2 \left(\frac{\lambda L_{3000}}{10^{37} \text{ W}} \right)^{0.62} \left(\frac{\text{FWHM}(\text{Mg II})}{\text{km s}^{-1}} \right)^2 \quad (1)$$

for the Mg II line and

$$\frac{M_{\text{BH}}}{M_\odot} = 4.6 \left(\frac{\lambda L_{1350}}{10^{37} \text{ W}} \right)^{0.53} \left(\frac{\text{FWHM}(\text{C IV})}{\text{km s}^{-1}} \right)^2 \quad (2)$$

for the C IV line. Here λL denotes the continuum luminosities at the specified wavelength and $\text{FWHM}()$ corresponds to the measured full width at half maximum of the spectral line.

3 DATA AND ANALYSIS

We are concerned with finding mean black hole masses for QSOs in the redshift bins shown in table 1. Since these predominantly cover redshift ranges where the $\text{H}\beta$ line is shifted off the end of the visible spectrum we exploit the methods of McLure & Jarvis (2002) and Vestergaard & Peterson (2006) for calculating these masses. To this end we require measurements of Mg II and C IV velocity widths, as well as monochromatic continuum luminosities near these lines (3000 Å and 1350 Å respectively). It should be noted that both of these UV mass estimators exhibit considerable scatter. It has been suggested that this may be intrinsic, possibly due to geometric considerations of the AGN (McLure & Dunlop 2002; Smith et al. 2002). However, in our analysis we make use of composite spectra created by combining all of the individual 2QZ spectra in the redshift bins (~ 2000 objects per bin). Composite spectra have several advantages. The high signal-to-noise they provide allows high precision in the measurement of line widths, and combining many spectra should average over intrinsic (e.g. geometric) variations.

In this section we briefly describe the 2QZ spectral data and our method for constructing composite spectra from them. We then discuss the process by which we measured the width of Mg II and C IV lines in the composites, and finally how we calculated the monochromatic luminosities λL_{3000} and λL_{1350} .

3.1 QSO spectra

All of the data in this paper come from the 2QZ and are described in detail elsewhere (Croom et al. 2004). The sample contains $> 23\,000$ spectra of QSOs in the magnitude range $18.25 < b_j < 20.85$ observed with the two-degree field instrument on the AAT. Spectra cover the wavelength range 3700–7900 Å with a dispersion of 4.3 Å pixel^{-1} and instrumental resolution of 9 Å . Spectra were typically observed for 3300–3600 s giving a median signal-to-noise ratio of $\sim 5.0 \text{ pixel}^{-1}$.

3.2 Composite spectra

The use of composite spectra is not a new technique (e.g. Francis et al. 1991; Vanden Berk et al. 2001) and a full description of our method for creating composites is given by

Croom et al. (2002). Here it is worth noting that 2QZ spectra are not flux calibrated. Therefore, to make the composites the individual spectra had to be normalised by fitting a polynomial continuum to regions without emission features. We then divide by this fitted continuum to uniformly normalise the spectra before combining. In doing so all information on continuum slope and normalisation is lost while the emission features remain intact. The normalised spectra were then shifted to the rest frame and the composites were constructed as the median of all contributing QSOs in each pixel (of width 1 \AA). Errors were determined by taking the 68 per cent semi-interquartile range of individual QSO pixel values.

3.3 Measurement of Line Widths

Before we measured emission line widths from our composite spectra, we had to correct for QSO iron emission. This correction was performed iteratively. A smoothed template of QSO iron emission (Vestergaard & Wilkes 2001) and linear continuum were fitted to the data in regions either side of the emission line in question. The iron template and continuum were then subtracted from the data, and a single Gaussian profile was fitted to the remaining line. In the case of C IV two other Gaussians were also fitted to the He II/O II] feature just redwards of the line. The iron template and continuum were then fitted to the spectrum again, this time excluding any data within the primary emission line region (defined as $\pm 3\sigma$ of the Gaussian fit to the line) and in the case of C IV with the two other Gaussians (defining the He II/O II] flux) subtracted from the data. This process was repeated until the width of successive Gaussian fits to the line differed by less than half their associated error. It is worth noting here that the Gaussian we fit to the primary emission line is not used to measure its width but only as a mask. Neither the Mg II nor the C IV line are well described by a single Gaussian, instead this allows us to define the parts of the spectrum unaffected by the emission line to use in our subsequent iron/continuum fit. Using this method we found that we could accurately remove the local emission features around both of these emission lines without making preliminary assumptions as to their width (see Fig. 1).

Once the iron emission had been subtracted from the spectra it was possible to measure the width of the lines. Our method for measuring line widths is similar to that used by Wang, Lu & Zhou (1998) in that we model each line's profile with a set of Gaussian components. We then take the FWHM of this model as our line width. We found this process to be more robust than reading the FWHM directly from the data which can be significantly affected by a single pixel, and a better indicator of the true FWHM than attempting to impose a profile on the line such as a single Gaussian or Lorentzian.

Since the Mg II line is symmetric we can accurately model its profile with two Gaussians. During the fitting process we tie the central wavelength of the Gaussians together but all other parameters (five in total: the central wavelength of the line and, the width and amplitude of each Gaussian component fit to the line) were left free. The asymmetry of the C IV line requires that we use three Gaussians to accurately model its profile with all nine parameters left free in the fitting process. In each case the multi-Gaussian models

were fit to the data using the MRQMIN routine (Press et al. 1989). At each step in the above fitting we take into account the propagation of errors through the process, and we reevaluate the error at each pixel taking into account uncertainty in the iron and continuum fits. The errors on the FWHM measurements could then be calculated analytically from the covariance matrix of the multi-Gaussian fit. Fig. 1 illustrates the line fitting process for both Mg II and a C IV. The multiple Gaussian components (two for Mg II and three for C IV) provide accurate models for the emission lines.

After each line width had been measured we corrected for the resolution of the spectrograph (9 \AA rest frame) by subtracting it in quadrature from the measured line width.

In calibrating equations 1 and 2 McLure & Dunlop and Vestergaard & Peterson define their FWHMs in different ways. Since r in the virial equation defines the radius of the broad-line region surrounding AGN McLure & Dunlop correct for narrow line Mg II emission, and take the FWHM of only the the broad component of the line to calibrate equation 1. However, in their analysis of broad UV lines in QSO spectra Wills et al. (1993) found no evidence for a narrow contribution to these lines. Therefore, Vestergaard & Peterson (2006) measure the FWHM of the entire C IV line when calibrating equation 2.

McLure & Dunlop (2004) model the Mg II line with a broad and narrow component following a similar procedure to that which we have outlined above. They then record the width of the broader component of the line to use in their calculations. However, in their fitting they impose the additional conditions that the velocity width of the narrower component of the line be $< 2000 \text{ km s}^{-1}$, and that the equivalent width of the narrower component be less than one third the equivalent width of the broad component. We do not apply these constraints in our fitting process and find that, while the narrower components all have equivalent width less than $1/3$ that of the broad, in all but one composite the width of the narrower Mg II component is $> 2000 \text{ km s}^{-1}$. If we were to add this additional constraint to the fitting procedure it would degrade the quality of the line fits, although we find this effect is small. Wills et al. (1993) find no evidence for a narrow line component in the Mg II line in QSO spectra and we find no reason to subtract off this 'narrower' contribution to the line. We also note that the use of Gaussians in our fitting process is somewhat arbitrary and hence it is difficult to assign a physical meaning to each of the components individually. We thus use the FWHM of the whole line in our calculations for Mg II (this may introduce systematic errors to our calculations, see section 3.5).

Note that the asymmetry of the C IV line (bottom-right panel Fig. 1) is of concern to this analysis. Other investigations of UV QSO spectra have shown that the C IV line is often found to be blueshifted with respect to lower ionisation lines such as Mg II (e.g. Marziani et al. 1996), and Richards et al. (2002) suggested that this may imply the C IV emitting region is outflowing from the AGN and hence not be fully virialised. However, our C IV line profiles do not resemble those in composite spectra constructed by Richards et al. for QSOs with blueshifted C IV. The asymmetry we observe in the C IV line could be caused by a range of possible physical processes including emission and/or absorption by non-virialised gas, however, a full discussion of this is beyond the scope of this investigation.

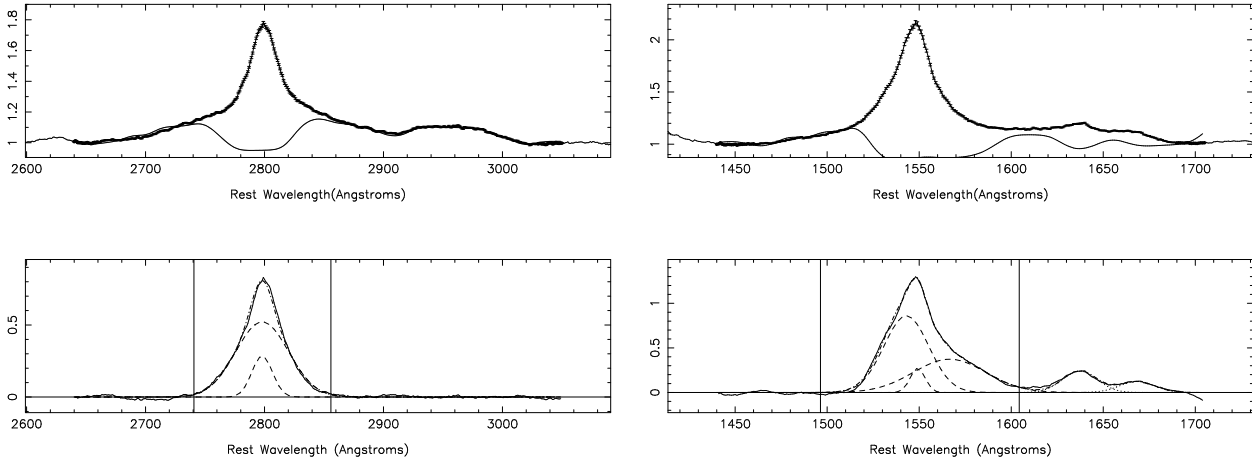


Figure 1. Illustrations of the line fitting procedures for Mg II (left) and C IV (right) in two of the composite spectra, note we observe very little variation in the line profiles between composites. In each case the top panel shows the initial composite spectrum and the smoothed iron template fitted to it. The lower panels show the spectrum after the iron emission was subtracted from it. Also shown in the bottom panels are the Gaussians used to model the line (dashed), as well as Gaussians used to fit other local emission features (dotted) and the sum of these for comparison with the composite (dash-dot; which follows closely the solid line). Vertical lines in the bottom panels indicate the regions outside of which the iron template was fit to our data. 68% interquartile errors for each point in the composite spectra are shown in the upper panels (these are hardly visible) but are omitted from the lower for clarity. For each spectrum the y axis denotes F_λ in arbitrary units of flux density.

On the other hand, we note that the original C IV line (top-right panel Fig. 1) shows no obvious asymmetry. The asymmetry then becomes pronounced after the iron template has been subtracted from the data. Therefore, it is possible that the asymmetry we observe may not be caused by any physical process in the QSOs, but by bad iron subtraction. Vestergaard & Wilkes (2001) make note when creating the template that iron emission in the vicinity of the C IV line can be difficult to isolate. The iron template is based on spectra of the Seyfert I galaxy I Zwicky 1, which shows considerable Si II emission bluewards of the C IV line. The C IV line itself is unusually weak, making it difficult to deblend the carbon, silicon and iron emission. Vestergaard & Wilkes (2001) find no emission directly redwards of the C IV line, and hence the iron template is asymmetric about this line. It is therefore unclear whether the asymmetry of the C IV line after the iron emission has been subtracted is real. We find no evidence of Si II emission in any of our composites, and it may be that this iron template is simply not applicable in this case.

We thus took note of the effect of the iron subtraction on our data. We repeated our analysis but instead of fitting an iron template along with a continuum to the data, we simply used a linear continuum fit between the approximate extremities of the C IV line (1500 Å and 1600 Å). We found this gave us FWHMs which were consistently smaller by a factor ~ 1.3 , however, the symmetry of the line remained intact in this procedure. In the analysis that follows we only use data measured after we had corrected for iron emission. Equation 2 was calibrated with line widths measured after correcting for iron emission, and we find that the template does accurately fit our composite spectra outside the immediate C IV line region.

3.4 Luminosity Measurements

The absolute magnitudes quoted in this paper (M_{b_J}) come from photographic observations in the b_J band with the UK Schmidt. These are corrected for extinction by Galactic dust (Schlegel, Finkbeiner, & Davis 1998), and K -corrected using the values provided by Cristiani & Vio (1990). To then calculate continuum luminosities at the wavelengths desired we made use of the Sloan Digital Sky Survey (SDSS) QSO composite spectrum (Vanden Berk et al. 2001). We first calculated the mean redshift and b_J luminosity of the QSOs in our composite which contributed to the spectral line we were analysing. Then the SDSS composite was redshifted to \bar{z} , and normalised to the measured luminosity in the b_J band by convolving with the UKST b_J response function. Then it was possible to read off values for L_{1350} and L_{3000} .

The magnitudes listed in the 2QZ are generally accurate to 0.1–0.2 magnitudes. Correcting for dust and K -correcting could introduce significant uncertainty into the values for M_{b_J} . However, once averaged over all ~ 2000 QSOs in a redshift bin we assume the error on \bar{M}_{b_J} will be negligible. On the other hand the extrapolation to L_{1350} and L_{3000} could be a significant source of error as we discuss below.

3.5 Errors

There are three possible sources of error to our calculations for M_{BH} . These are errors in the luminosity values, errors in the line width measurements and intrinsic scatter associated with equations 1 and 2.

Equations 1 and 2 are quoted as having errors of 0.33 dex and 0.36 dex respectively (McLure & Dunlop 2004; Vestergaard & Peterson 2006), and as we shall see these large scatters dominate the random error in M_{BH} . It is worth noting here that since the quoted errors are rms values and because we are dealing with large numbers of objects (~ 2000 QSOs per redshift bin), it could be argued that the errors

should be reduced by the according factor ($\sim 1/\sqrt{2000}$). However, the large error in the virial mass estimators is to a large extent due to the limited number of AGN with reliable mass estimates from reverberation mapping. Since the calibrations are based only on a few tens of objects, we do not believe it to be prudent to be reducing the errors in our calculations because of the large number of objects in our dataset.

The high signal to noise of composite spectra mean that very precise line widths can be measured. We calculate errors on these widths analytically from the covariance matrix of the fitting parameters described in section 3.3, and find them to be negligible (see table 1). However, the process by which we measure line widths could introduce significant systematic errors to our calculations. One source of uncertainty is the nature of the iron template we used and how it was fit to our data. We note above that the asymmetry we observe in the C IV line may be a product of the iron template we are using, and we cannot be sure that using this iron template doesn't introduce errors into the line width measurements. We find that if we simply fit a linear continuum around the C IV line our results are reduced by ~ 1.3 . We therefore gauge that any problems with the iron template will have an effect no greater than this on our line width measurements, or a factor of ~ 1.7 in our virial black hole masses.

Another source of uncertainty in our line width determinations is narrow line emission. None of the spectral lines analysed show clear signs of narrow line emission. Their profiles are smooth and do not exhibit the inflection characteristic of narrow line emission superimposed on a broad line. Indeed other investigations of the UV lines in QSO spectra have found no evidence that they contain narrow line cores (Wills et al. 1993). However, as stated above McLure & Dunlop only consider the broader component of the Mg II line when calibrating equation 1 while we measure the FWHM of the whole line. In doing so we may introduce systematics to our calculations. We consider the possible effect of this by recording the width of the broader component of the modelled Mg II fit. We find that line widths measured this way are ~ 1.5 times larger than those measured for the whole line which translates to roughly a factor of 2 in M_{BH} .

Extrapolating luminosities in the manner described above can often be a large source of error in calculations, in particular when performed on single objects. In our case, however, we are calculating average luminosities for the ~ 2000 QSOs in each redshift bin. Thus using the flux calibrated SDSS composite, itself constructed from > 2000 QSO spectra in the redshift range we are investigating, should introduce only small errors into the luminosity calculations. The SDSS median QSO composite has a continuum described by $F_\lambda \propto \lambda^\alpha$ with $\alpha = -1.54$ for $\lambda < 5000 \text{ \AA}$ and $\alpha = -0.42$ for $\lambda > 5000 \text{ \AA}$. Power laws with $-2 < \alpha < -1.5$, are used throughout the literature to make extrapolations similar to those we make. Therefore we also evaluate the monochromatic luminosities assuming these power laws and define the error on our luminosity values to be half their difference.

We calculate the errors on the virial mass estimates taking into account the scatter in the virial mass estimators as well as errors in our luminosity calculations and line width measurements. However, the the final error on the mass es-

timate is completely dominated by the uncertainty in the mass estimator. We do not attempt to account for possible sources of uncertainty from poor iron subtraction or narrow line emission in the tabulated errors.

4 DARK HALO MASS

Croom et al. (2005) used measurements of the clustering of QSOs from the 2QZ to infer the mass of dark matter haloes that they inhabit. They divide the 2QZ sample into 10 redshift intervals (see table 1) each containing ~ 2000 QSOs and measure the two-point correlation function (accounting for redshift-space effects) on $< 20 h^{-1}$ Mpc scales. They then compare this to the evolution of mass clustering in a WMAP/2dF cosmology (Spergel et al. 2003; Percival et al. 2002) to determine the bias of QSOs as a function of redshift. Note that Croom et al. (2005) use a slightly different cosmology in their calculations: $(\Omega_m, \Omega_\Lambda) = (0.27, 0.73)$ and $H_0 = 73 \text{ km s}^{-1} \text{ Mpc}^{-1}$, although we do not expect these slight differences to have a significant affect on our calculations.

Finally they use the formalism developed by Mo & White (1996) to relate bias and dark matter halo mass, specifically using the relation for ellipsoidal collapse given by Sheth, Mo & Tormen (2001). This results in the finding that 2QZ QSO hosts have approximately the same dark matter halo mass as a function of redshift, with $M_{\text{DH}} = (3.0 \pm 1.6) \times 10^{12} h^{-1} M_\odot$. Croom et al. (2005) then use a range of partly theoretical relationships between M_{BH} and M_{DH} to derive black hole masses for these QSOs (see Eqs 22-26 in Croom et al 2005). In all cases the black hole masses are seen to decrease toward lower redshift. This so called *cosmic downsizing* (see also Barger et al. 2005; Heckman et al. 2004) appears to be driving QSO luminosity evolution at $z < 2.5$. However, in order to demonstrate this more conclusively, we have undertaken the analysis in the present paper to determine more directly the black hole masses of 2QZ QSOs (building on the previous work of Corbett et al. 2003).

5 RESULTS

Table 1 displays the results of our analysis and in Fig.2a we show the virial black hole mass estimates as a function of redshift. A clear 'step' is visible where we switch from Mg II estimates to C IV. In addition, for one redshift bin we have both Mg II and C IV present in the composite spectra, and for this bin the calculated values of M_{BH} differ by just over 1σ . This disagreement is only marginally significant but does raise questions over the calibrations of equations 1 and 2. However, since these two relations are not inter-calibrated we should not be surprised that we find some discrepancy. We also note that the magnitude of this offset is consistent with the systematic errors discussed in section 3.5. Hereafter we use the weighted mean of the two mass estimates for the redshift bin $z \in (1.50, 1.66)$: $\text{Log}(\frac{M_{\text{BH}}}{M_\odot}) = 8.7 \pm 0.35$.

We note here that the H β line is present in the composite spectrum for redshift bin $z \in (0.30, 0.68)$. We could therefore obtain a virial black hole mass estimate for this bin from the H β line following a calibration by e.g. Vestergaard

& Peterson (2006). Comparing this with the Mg II mass estimate for the same redshift bin could help tie the calibrations together, and potentially clarify why we observe the difference between the Mg II and C IV estimators. However, we found that procedures for measuring the width of the H β line were not well defined in the literature. In particular other authors have found evidence for a ‘very broad component’ to the H β line (e.g. Marziani 2003) which could have a large effect on our measurements. In addition, because of the nature of composite spectra the same set of individual QSO spectra do not contribute to the H β and Mg II lines in a single composite (note this is equally true for the C IV and Mg II lines in composite $z \in (1.50, 1.66)$). Due to the above considerations, and because we would only obtain a single point to compare with our Mg II measurements, we do not make an estimate of the virial black hole mass for the first redshift bin from the H β line.

It is interesting to note that the line widths in table 1 hardly vary between the composites. Given that this is the case any variation observed in M_{BH} must be due to the luminosity. Thus the flux limits of the 2QZ ($18.25 < b_J < 20.85$) will effectively impose limits on the masses we have calculated. We can estimate these limits by calculating the black hole mass as a function of redshift, given a source with an average line width and an apparent magnitude at the upper and lower limits of the survey. We show these limits in Fig.2a and it appears that these confine our average black hole masses to only a very small range of possible values at any given redshift. It is worth noting that the upper flux limit of the 2QZ does not have a tremendous effect on our calculations. Croom et al. (2004) extended the 2QZ to a b_J of 16 in the 6dF QSO Redshift survey (6QZ) and found an extra ~ 320 QSOs in roughly half the area of sky as surveyed in the 2QZ. Considering the comparatively small numbers of these bright QSOs, we do not believe they could contribute significantly to our composite spectra. The lower flux limit, however, does clearly affect our results. Thus we do not present Fig.2a as evidence for evolution in black hole mass for the global QSO population. Instead this shows average virial black hole mass estimates for QSOs in the 2QZ between redshift 2.5 and 0.5.

5.1 The $M_{\text{BH}} - M_{\text{DH}}$ relation

Correlations between black hole mass and galactic properties locally imply that massive black holes grow in parallel with the galaxies (and presumably dark matter halos) in which they reside. Thus we expect M_{BH} and M_{DH} to be related. Ferrarese (2002) proposed three such relations based the local $M_{\text{BH}} - \sigma$ relation and different models for the dark matter halo density profile. In brief the first assumes an isothermal dark matter profile, the second assumes an NFW profile (Navarro, Frenk, & White 1997), and the third assumes a profile based on the weak lensing results of Seljak (2002). In each of these models the dark halo mass is calculated from an estimate for the halo virial velocity v_{vir} which cannot be directly measured for dark matter halos. Hence Ferrarese extrapolates from the galaxy’s circular velocity, v_c , to v_{vir} using the above density profiles. This is a large extrapolation and the source of the offset between the models. We combine the models with two assumptions concerning the evolution of this relation (see Wyithe & Loeb 2005; WL05), namely

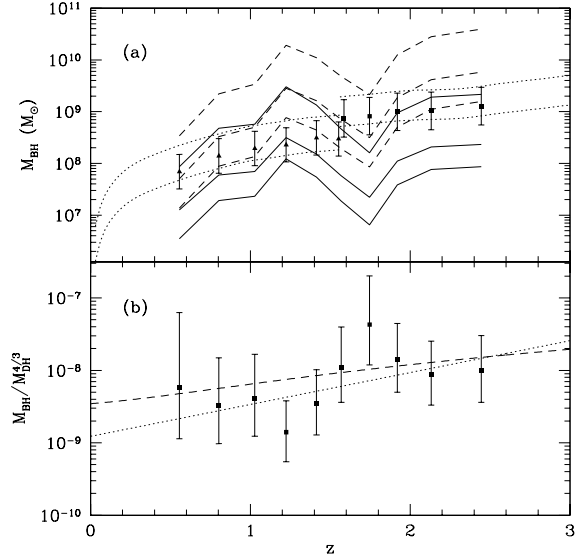


Figure 2. (a) The trend in virial M_{BH} estimates with redshift. The difference between the Mg II (triangles) and C IV (squares) results is well illustrated here. We also show approximate limits on our black hole mass estimates as imposed by the flux limits of the 2QZ assuming an average line width (dotted lines). In addition $M_{\text{BH}}(M_{\text{DH}})$ estimates calculated assuming various dark matter halo density profiles with no evolution in the $M_{\text{BH}} - M_{\text{DH}}$ relation (solid lines) and evolution $\propto (1+z)^{2.5}$ (dashed lines) are shown. For each model the calculations assuming an isothermal density profile give the lowest estimates for M_{BH} , the intermediate estimates are given by an NFW profile, and the Seljak model gives the highest. Note that we do not present the errors on these points for clarity. (b) We show our values for $M_{\text{BH}}/M_{\text{DH}}^{4/3}$ (squares) compared with the predictions of Robertson (2005) (dashed line). We also show our best fit to the data (dotted line).

that $M_{\text{BH}} - M_{\text{DH}} \propto (1+z)^{2.5}$; dashed lines in Fig.2a) and $M_{\text{BH}} - M_{\text{DH}}$ is constant with z (solid lines in Fig.2a).

Table 2 summarises the results of χ^2 analysis comparing the black hole masses derived from the dark halo mass, $M_{\text{BH}}(M_{\text{DH}})$, to our virial black hole masses. That is, a comparison between our data points and the solid/dashed lines in Fig.2a allowing for the errors on the estimate of $M_{\text{BH}}(M_{\text{DH}})$ (which, for clarity, are not shown in Fig. 2a). The comparison was done in log-space and (for non-symmetric errors) took the error on $M_{\text{BH}}(M_{\text{DH}})$ in the direction of the virial M_{BH} estimates. The errors are not normally distributed, and hence our results here are a guide rather than being statistically robust. However, it appears that the ‘ $M_{\text{BH}} - M_{\text{DH}}$ constant’ model with an isothermal profile is rejected by the data, while the others are reasonably acceptable (i.e. cannot be rejected at the 85% level).

Recent hydrodynamical simulations of galaxy mergers have shown that the local $M_{\text{BH}} - \sigma$ relation, along with a startling array of other QSO features, can be reproduced under the condition that QSO energy feedback self-regulates the growth of massive black holes (eg: Di Matteo et al. 2005; Robertson et al. 2005; Hopkins et al. 2005). These simulations predict an $M_{\text{BH}} - \sigma$ relation of the form

Table 1. Each line represents measurements taken from one spectral line (Note that the composite spectra for redshift bin $z \in (1.50, 1.66)$ had both the C IV and Mg II lines visible). For each line we give the average redshift and absolute b_J magnitude of QSOs contributing to the composite spectra at that line, along with the absolute magnitude of the break in the QSO luminosity function at that redshift $M_{b_J}^*$ (Assuming the polynomial evolution model of Croom et al. 2004). Note that the values for \bar{z} and \bar{M}_{b_J} vary at each point in a single composite spectra because at each point there will be a different group of spectra contributing to the composite. We also present the measured FWHMs for the lines and monochromatic luminosities near them 3000 Å and 1350 Å for Mg II and C IV respectively). We give the black hole mass calculated from the line and derived Eddington ratios (L/L_{Edd}) and finally the dark halo masses calculated by Croom et al. (2005).

z interval	\bar{z}	\bar{M}_{b_J}	$M_{b_J}^*$	Spectral Line	FWHM (km s^{-1})	$\text{Log}(\frac{\lambda L}{W})$	$\text{Log}(\frac{M_{\text{BH}}}{M_{\odot}})$	$\text{Log}(L/L_{\text{Edd}})$	$\frac{M_{\text{DH}}}{\times 10^{12} M_{\odot}}$
0.30,0.68	0.556	-22.28	-23.30	Mg II	3546 ± 19	37.379 ± 0.001	7.8 ± 0.33	-0.71 ± 0.33	$1.15^{+2.18}_{-0.94}$
0.68,0.92	0.803	-23.26	-23.91	Mg II	3875 ± 14	37.747 ± 0.017	8.1 ± 0.33	-0.64 ± 0.33	$2.94^{+3.07}_{-1.83}$
0.92,1.13	1.028	-23.85	-24.39	Mg II	3878 ± 15	37.977 ± 0.030	8.3 ± 0.33	-0.56 ± 0.33	$3.25^{+3.14}_{-1.93}$
1.13,1.32	1.224	-24.26	-24.75	Mg II	3783 ± 16	38.127 ± 0.040	8.4 ± 0.33	-0.48 ± 0.33	$8.11^{+4.08}_{-3.11}$
1.32,1.50	1.414	-24.57	-25.04	Mg II	4104 ± 18	38.229 ± 0.049	8.5 ± 0.33	-0.50 ± 0.33	$5.20^{+3.15}_{-2.28}$
1.50,1.66	1.552	-24.75	-25.22	Mg II	3889 ± 31	38.272 ± 0.055	8.5 ± 0.33	-0.41 ± 0.33	$2.89^{+2.27}_{-1.51}$
1.50,1.66	1.585	-24.80	-25.26	C IV	5438 ± 58	38.394 ± 0.031	8.9 ± 0.36	-0.79 ± 0.36	$2.89^{+2.27}_{-1.51}$
1.66,1.83	1.746	-25.03	-25.42	C IV	5444 ± 44	38.472 ± 0.024	8.9 ± 0.36	-0.75 ± 0.36	$1.62^{+1.75}_{-1.01}$
1.83,2.02	1.919	-25.25	-25.56	C IV	5687 ± 40	38.564 ± 0.017	9.0 ± 0.36	-0.75 ± 0.36	$4.30^{+2.61}_{-1.89}$
2.02,2.25	2.132	-25.46	-25.67	C IV	5629 ± 39	38.609 ± 0.010	9.0 ± 0.36	-0.69 ± 0.36	$6.28^{+3.10}_{-2.37}$
2.25,2.90	2.445	-25.83	-25.71	C IV	5707 ± 39	38.763 ± 0.001	9.1 ± 0.36	-0.64 ± 0.36	$6.73^{+3.77}_{-2.80}$

Table 2. Comparisons of χ^2 statistics for the different models shown in Fig. 2a. Note that since errors on M_{DH} are not normally distributed this χ^2 analysis is not statistically robust. We present it here as a guide to how well each model matches our data.

Model	Assumed dark matter halo density profile	χ^2	$P(> \chi^2)$
$M_{\text{BH}} - M_{\text{DH}}$ const.	Isothermal	24.1	0.01
	NFW	14.1	0.17
	Seljak	5.0	0.89
$M_{\text{BH}} - M_{\text{DH}}$ $\propto (1+z)^{2.5}$	Isothermal	5.4	0.86
	NFW	6.7	0.75
	Seljak	13.4	0.20

$$\log\left(\frac{M_{\text{BH}}}{M_{\odot}}\right) \approx 8.1 + 4.0 \log\left(\frac{\sigma}{200 \text{ km s}^{-1}}\right) - 0.19 \log(1+z). \quad (3)$$

We take $\sigma \approx V_{\text{vir}}$ (see Fig. 3 of Di Matteo et al. 2005) where V_{vir} is the virial velocity in the simulations and is directly related to the total galaxy mass by $M_{\text{DH}} \approx M_{\text{vir}} = V_{\text{vir}}^3 / 10 G H(z)$. Assuming the cosmological parameters specified in section 1 this gives us a redshift dependent relationship between M_{BH} and M_{DH} characterised by

$$\log\left(\frac{M_{\text{BH}}}{M_{\odot}}\right) \approx -8.5 + \frac{4}{3} \log\left(\frac{M_{\text{DH}}}{M_{\odot}}\right) - \log\left(\frac{(0.7 + 0.3(1+z)^3)^{\frac{2}{3}}}{(1+z)^{0.19}}\right). \quad (4)$$

We show their predictions for $M_{\text{BH}}/M_{\text{DH}}^{4/3}$ as a function of redshift in Fig. 2b along with our calculated values. We find good agreement between the simulation predictions and our values. Our best fit to the data is also shown which follows $M_{\text{BH}}/M_{\text{DH}}^{4/3} \propto (1+z)^{2.5 \pm 1.8}$.

Fig. 3 shows the relation between M_{BH} and M_{DH} . We

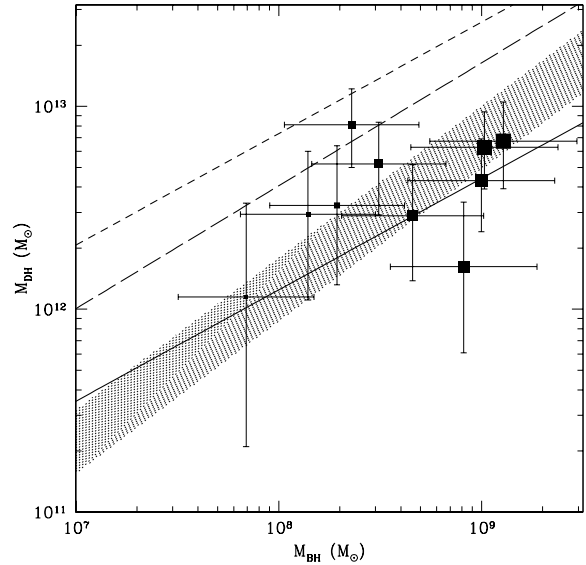


Figure 3. Shows our values for M_{BH} plotted against M_{DH} found by Croom et al. (2005). The size of the points are scaled by redshift (larger points for higher z). The $M_{\text{BH}} - M_{\text{DH}}$ relation of equation 4 is also shown as the shaded region in the plot, with the relation at $z = 0$ defining the top of the region and $z = 2.5$ defining the bottom. The $z = 0$ $M_{\text{BH}} - M_{\text{DH}}$ relations of Ferrarese (2002) are also shown (heavy lines) for the isothermal (short dash), NFW (long dash) and Seljak (solid) density profiles.

observe a weak correlation between these values significant at only the 85 per cent level (applying a Spearman rank test). The weakness of this correlation is due in part to the limited dynamic range of our averaged mass estimates. We also plot Eq. 4 between $z = 0.5$ and 2.5 as the shaded region in the Figure, and the $z = 0$ relations of Ferrarese (2002).

We see that the relation of Robertson et al. is in excellent agreement with our data. It is worth noting that the normalisation of the simulated curve (in both Fig. 2b and 3) comes only from the QSO luminosity function. It is therefore encouraging that the simulation's predictions for the $M_{\text{BH}} - M_{\text{DH}}$ relation match our measurements so well. The Ferrarese relation assuming a Seljak profile is also in good agreement with the data. However, the Ferrarese relations assuming other dark matter profiles appear to be in disagreement (particularly that with an isothermal profile, as noted above).

Fitting a function of the form $M_{\text{BH}} = AM_{\text{DH}}^{1.82}$ to the data in Fig. 3, we estimate the zero-point of the $M_{\text{BH}} - M_{\text{DH}}$ relation in our redshift range to be $M_{\text{BH}} = 10^{8.4 \pm 0.2} M_{\odot}$ at $M_{\text{DH}} = 10^{12.5} M_{\odot}$. This estimate was obtained through minimising $\chi^2(A)$ for the fitted function, and the confidence interval represents $\Delta\chi^2 = 1$ limits. The exponent in the fitted model was chosen as that from the Ferrarese relation assuming a Seljak profile. As a check we repeated the analysis with the most extreme exponents from the various other models discussed in this paper and found that all resulted in a zero-point within the confidence interval quoted. By comparison the Ferrarese relations at $z = 0$ give a zero-point of $M_{\text{BH}} = 10^{7.3}$, $10^{7.8}$ and $10^{8.7} M_{\odot}$ at the same dark matter halo mass for isothermal, NFW and Seljak profiles respectively. In agreement with the above, the relation using the Seljak profile is the best match to the data. Given the uncertainties in the evolution of the $M_{\text{BH}} - M_{\text{DH}}$ relation, this is not direct evidence for or against a specific dark matter halo profile. We also note that our zero-point for the $M_{\text{BH}} - M_{\text{DH}}$ is consistent with that found for a small sample of QSOs (but with larger dynamic range) by Adelberger & Steidel (2005).

5.2 Bias in the measured $M_{\text{BH}} - M_{\text{DH}}$ relation

In addition to the random errors associated with the values of mean black hole mass and dark halo mass that we deduce, we should also consider whether there are any systematic biases that may arise in our analysis of the $M_{\text{BH}} - M_{\text{DH}}$ relation. Biases due to the uncertainties in the estimates of M_{BH} are discussed above. However, there is one further issue that is particularly important if we wish to compare with relations such as those of Ferrarese (2002) at low redshift.

Ferrarese draws her objects from a sample of local galaxies with measured black hole masses. These are fairly evenly distributed over a range of bulge (and hence inferred dark halo) masses. On the other hand, our QSO sample is drawn from the population of active galaxies, selected by luminosity. This tends to produce a Malmquist-type bias towards larger M_{BH} . If we consider that, at a given redshift, objects will only be detected above a given M_{BH} mass (neglecting for the moment variation in Eddington ratio), then the mass function of dark matter halos (with more halos at low mass) and any scatter in M_{BH} for a given M_{DH} will cause an excess of objects above the fiducial $M_{\text{BH}} - M_{\text{DH}}$ relation (i.e. with greater M_{BH}). This leads to a bias of the observed mean value of M_{BH} above the true $M_{\text{BH}} - M_{\text{DH}}$ relation. Allowing there to also be scatter in the L/L_{Edd} relation is equivalent to moving the effective M_{BH} limit, and only moves the observed zero-point of the $M_{\text{BH}} - M_{\text{DH}}$ relation parallel to the true relation.

The size of the Malmquist-type bias depends on both

the steepness of the mass function and the amount of intrinsic scatter in the relationship between black hole and dark halo mass. Both these quantities are rather uncertain, but we can estimate the possible size of the effect in the following way. First, we assume the same mass function of dark halos that was assumed when deducing the clustering bias that led to the inferred mean dark halo mass: namely a Sheth et al. (2001) mass function with the cosmological parameters assumed in this paper. Then, we assume that the black hole mass function may be generated from the dark halo mass function by applying the Ferrarese relation, either with no evolution or with WL05 evolution in the mass relation, but with some scatter in that relation. Constructing a Monte-Carlo simulation of the $M_{\text{BH}} - M_{\text{DH}}$ relation as outlined above, and including a cutoff in black hole mass corresponding to the flux limit of the 2QZ we can find the magnitude of this effect on our results. Note that a cut in M_{BH} will also cause us to overestimate the gradient of the relation. However, due primarily to the small dynamic range in Fig. 3, we make no attempt to estimate the slope of the $M_{\text{BH}} - M_{\text{DH}}$ relation in this work. We are concerned only with the zero-point of the relation, which is also biased by the cut.

We test three values of scatter in the $M_{\text{BH}} - M_{\text{DH}}$ relation. The minimum scatter we adopt is the scatter between black hole mass and bulge velocity dispersion or luminosity inferred by Marconi et al (2004), namely a factor of 2 in black hole mass. However, there is likely to be substantial additional scatter in the relation between bulge mass and dark halo mass: from Ferrarese (2002) we estimate the total scatter could be a factor 4 in black hole mass although without direct measurements of dark halo mass this is difficult to assess reliably. Table 3 shows the mean black hole masses after correcting our measured values for this Malmquist-type bias in each redshift bin for the two different evolutionary models and three different values of the scatter in the $M_{\text{BH}} - M_{\text{DH}}$ relation, namely $\times 2$, $\times 4$ and $\times 10$. Although we estimate above that the scatter should be between a factor of 2 and 4, the uncertainties are great enough that it is worth considering the affect of a larger scatter (i.e. $\times 10$).

The biases for the two evolution assumptions are similar, with the WL05 evolution producing slightly less bias at high masses and high redshift, as in this case the associated dark halo mass is lower for a given black hole mass (and so the mass function is flatter). For the minimum scatter assumption, the bias is ~ 0.1 dex. For $\times 4$ scatter, however, the bias increase to a factor ~ 0.25 dex or greater. If we now consider the zero-point for the $M_{\text{BH}} - M_{\text{DH}}$ relation derived above, we see that any Malmquist bias will push the true zero-point to lower M_{BH} .

We note that the true scatter in the $M_{\text{BH}} - M_{\text{DH}}$ is very poorly constrained. If it were to be considerably higher than the above values, then the Malmquist bias would also be higher. A scatter of a factor of 10 in M_{BH} for a given M_{DH} will produce a bias of ~ 0.6 dex in the mean M_{BH} with respect to the true $M_{\text{BH}} - M_{\text{DH}}$ relation. This would make our data inconsistent with the Robertson et al. (2005) model (Eq. 4) and the Ferrarese (2002) model assuming a Seljak (2002) density DMH profile, while giving better agreement with the NFW profile model in particular. Hence a detailed comparison of the high-redshift relation deduced here and the relation at lower redshifts found by Ferrarese (2002) re-

Table 3. Estimates of Malmquist bias in the mean M_{BH} measured relative to the true $M_{\text{BH}} - M_{\text{DH}}$ relation. For each redshift bin at \bar{z} , we give the measured M_{BH} (column 2) and the corrected values assuming the three values of intrinsic scatter about the mass relation ($\times 2$, $\times 4$ and $\times 10$), for each of the two assumed values for evolution (columns 3 to 8). M_{BH} is given as $\log_{10}(M)$ in solar units. The final row gives the zero-point calculated as described in the text. The error on these zero-points are ± 0.22 dex.

\bar{z}	no evolution				WL05 evolution		
	zero scatter	$\times 2$ scatter	$\times 4$ scatter	$\times 10$ scatter	$\times 2$ scatter	$\times 4$ scatter	$\times 10$ scatter
0.556	7.8	7.75	7.61	7.26	7.74	7.59	7.25
0.803	8.1	8.04	7.90	7.53	8.05	7.90	7.56
1.208	8.3	8.24	8.08	7.72	8.25	8.10	7.74
1.224	8.4	8.35	8.19	7.81	8.35	8.18	7.84
1.414	8.5	8.44	8.26	7.88	8.44	8.27	7.91
1.552	8.5	8.44	8.26	7.88	8.44	8.28	7.91
1.585	8.9	8.83	8.64	8.24	8.84	8.67	8.29
1.746	8.9	8.83	8.64	8.23	8.85	8.68	8.30
1.919	9.0	8.94	8.74	8.32	8.95	8.77	8.39
2.132	9.0	8.94	8.72	8.28	8.94	8.75	8.35
2.445	9.1	9.01	8.77	8.32	9.02	8.84	8.44
z-p	8.4	8.33	8.14	7.74	8.33	8.16	7.79

quires a better understanding of the amount of Malmquist bias in the QSO measurements, and in particular of the amount of scatter on the $M_{\text{BH}} - M_{\text{DH}}$ relation.

5.3 The evolution in M_{BH} and L/L_{Edd}

Fig. 2a displays evidence for a trend in estimated black hole mass with z as we observe M_{BH} for our sample to drop by an order of magnitude between redshift 2.5 and 0.5. The correlation between M_{BH} and z is significant at the 99% level (via a Spearman rank test; i.e. the probability that the null hypothesis of no correlation is correct is $< 1\%$) and the evolution in M_{BH} is best characterised by $M_{\text{BH}} \propto (1+z)^{3.9 \pm 1.1}$. However, due to the flux limits of the 2QZ we can not use this to infer black hole mass evolution in the global QSO population (see section 5).

In our sample the flux limit of the 2QZ and the luminosity evolution of QSOs conspire to put L^* at a similar apparent magnitude at every redshift we sample. The mean luminosity of our sample (i.e. the third column of Table 1) scales as $(1+z)^4$ while L^* scales as $(1+z)^3$ (Table 1 lists the break in the QSO luminosity function, $M_{b_j}^*$ at the mean redshift of each bin using the polynomial form of Croom et al. 2004), so that the range of differences between L and L^* for our sample is equivalent to 1 magnitude. We also note that the space density of the QSOs in our redshift bins changes by only a factor of 2.7 (Croom et al. 2005) over our redshift range. However, the strong luminosity dependence of the virial black hole mass estimators, combined with this evolution in L^* , make untangling luminosity and mass evolution difficult. Indeed the evolution we observe in BH mass is entirely due to the luminosity component of the virial mass estimator as the velocity widths show no significant trend with redshift. In principle QSOs in our sample could have shown evolution in their emission line FWHM to alter the

Table 4. Summary of analysis on our sample of QSOs defined by a constant magnitude interval around $M_{b_j}^*$. Column 3 shows the difference between the average magnitude of the QSOs in that bin and $M_{b_j}^*$. Note that for all but the final redshift bin this is nearly constant, the final redshift bin (and the first) is affected by the magnitude limits of the 2QZ.

\bar{z}	\bar{M}_{b_j}	$\bar{M}_{b_j} - M_{b_j}^*$	$\text{Log}(\frac{M_{\text{BH}}}{M_{\odot}})$	$\text{Log}(L/L_{\text{Edd}})$
0.568	-23.09	0.26	8.0 ± 0.33	-0.6 ± 0.33
0.807	-23.68	0.26	8.2 ± 0.33	-0.6 ± 0.33
1.030	-24.17	0.25	8.4 ± 0.33	-0.5 ± 0.33
1.225	-24.50	0.28	8.4 ± 0.33	-0.5 ± 0.33
1.416	-24.81	0.27	8.6 ± 0.33	-0.5 ± 0.33
1.566	-25.02	0.25	8.7 ± 0.35	-0.6 ± 0.35
1.746	-25.18	0.29	8.9 ± 0.36	-0.7 ± 0.36
1.920	-25.37	0.24	9.0 ± 0.36	-0.7 ± 0.36
2.135	-25.46	0.26	9.0 ± 0.36	-0.7 ± 0.36
2.431	-25.67	0.10	9.1 ± 0.36	-0.6 ± 0.36

evolution of M_{BH} , but this is not seen. The best approach to investigate BH mass evolution in the global QSO population would be to construct a sample with larger dynamic range in magnitude (Richards et al. 2005). This would allow sources of the same luminosity to be compared over a range of redshifts.

We therefore restrict our discussion of evolution to L^* QSOs. Since the 2QZ samples a range of luminosities around L^* at all redshifts, we can create a subsample defined by a luminosity interval around L^* which is not affected by the flux limits of the 2QZ. The range in magnitude of this sample is defined at the bright end by the absolute magnitude of a QSO at low redshift with an apparent magnitude of $b_j = 18.25$, and at the faint end by the absolute magnitude of a source at high redshift with $b_j = 20.85$. Note that at $z = 0.3$ (the lowest redshift in our sample) $M_{b_j}^* = -22.59$ (calculated using the polynomial evolution model of Croom et al. 2004). This corresponds to an apparent magnitude of $b_j = 18.15$, brighter than the flux limit of the 2QZ. Hence we define the boundaries of this sample by the absolute magnitudes corresponding to $b_j = 18.25$ at $z = 0.556$ and $b_j = 20.85$ at $z = 2.445$, i.e. at the mean redshift of the end bins. Thus the data for the end bins are still slightly affected by the magnitude limits of the 2QZ. This new sample is then described, at all redshifts, as all QSOs with

$$-0.62 < M_{b_j} - M_{b_j}^*(z) < 0.75. \quad (5)$$

We repeat the analysis described in this paper on this new sample to investigate the evolution of black hole mass in typical L^* QSOs. Composite spectra were made for the same redshift intervals, and virial black hole masses were estimated from these. Table 4 shows a summary of these results and they are plotted in Fig. 4a. We find $(1+z)^{3.3 \pm 1.1}$ evolution in M_{BH} , less pronounced than in the whole sample although still marginally significant. This shows that QSO samples at lower redshift are increasingly dominated by lower mass BH, but as these are also lower-luminosity QSOs this cannot directly be interpreted as evidence for anti-hierarchical "downsizing".

To further elucidate what may drive QSO luminosity evolution we calculate average Eddington ratios (L/L_{Edd})

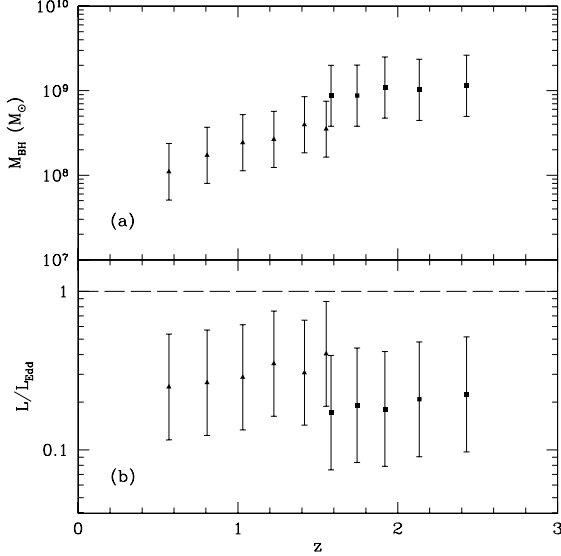


Figure 4. (a) Black hole masses as a function of redshift for the sample of L^* QSOs. (b) Eddington ratios calculated for the same sample. The dashed line represents $L/L_{\text{Edd}} = 1$. In each case triangles and squares represent measurements from the Mg II and C IV lines respectively.

for the QSOs in our redshift bins. In calculating the Eddington ratios bolometric luminosities (L) were found using the relation derived by McLure & Dunlop (2004) for the B band correcting by $b_J = B - 0.06$ for a mean QSO $B - V = 0.22$ (Cristiani & Vio 1990). The relation is then

$$M_{b_J} = -2.66 \log(L) + 79.42 \quad (6)$$

for L in watts. L_{Edd} (also in watts) is given by

$$L_{\text{Edd}} = 10^{39.1} \left(\frac{M_{\text{BH}}}{10^8 M_{\odot}} \right). \quad (7)$$

McLure & Dunlop arrive at this relation from the bolometric corrections of Elvis et al. (1994). Elvis et al. find an error on their B band bolometric correction of $\sim 35\%$, and all of their sample give a correction within a factor of ~ 2 of the mean. Even taking this factor of two as the error on our bolometric correction for a single object, when averaged over the ~ 2000 QSOs in a redshift bin this translates to a factor of only $2/\sqrt{2000} \sim 0.04$. This error is small when compared with those on our black hole mass estimates, and is ignored in the following analysis. Any luminosity dependence in the bolometric correction would introduce systematics into our results, however, Richards et al. (2006) find no evidence such a dependence.

Calculated Eddington ratios for the L^* QSOs are plotted in Fig. 4b. We observe no significant trend in Eddington ratio with redshift, characterised by $L/L_{\text{Edd}} \propto (1+z)^{-0.4 \pm 1.1}$, indicating that the most luminous QSOs that are typically observed in samples have similar Eddington ratios, irrespective of redshift. Overall, however, the mean rate of accretion in the universe must have been higher at high z , because the integrated luminosity arising from AGN was higher at high z than at low, whereas the integrated irreducible mass in black holes cannot have been greater at

high z than at low (see also Miller, Percival & Croom 2005). It seems then that the process of selecting luminous QSOs results in an almost invariant Eddington ratio for the most extreme objects at any epoch, although given both the statistical and systematic uncertainties present in Fig. 4b it is not yet possible to rule out some redshift variation of Eddington ratio for these objects.

Our results are consistent with no evolution in Eddington ratios over the redshift range studied. Instead we must conclude that the luminosity evolution of L^* QSOs is driven, at least for the most part, by a reduction in black hole mass for $z < 2.5$. This said the confidence intervals on our evolution parameters are large and we restrain from drawing any firm conclusions on evolution from these data. The relative contribution of mass and Eddington evolution are affected strongly in our data by the slope of the radius-luminosity relation used in the virial mass estimates and the possibility of luminosity/redshift dependence in velocity widths (which is small, see Corbett et al. 2003). In addition the calibration of the virial mass estimators also has a major affect on our results. These are not dependent on z and hence alterations to the calibrations would lead only to an offset in our mass estimates. However, since each calibration applies to a different range of redshifts, an offset to one of these calibrations will significantly change our evolution results. We note that had we performed the above analysis with older calibrations for the two mass estimators we would have found considerably less evolution in M_{BH} over this redshift range, and a correspondingly larger evolution on Eddington ratios.

6 CONCLUSIONS

We make composite spectra of QSOs from the 2QZ to find average virial black hole mass estimates for the QSOs in 10 redshift bins for which Croom et al. (2005) had already calculated M_{DH} via clustering analysis. Comparing the black hole and dark halo masses we find evidence for $\sim (1+z)^{2.5 \pm 1.8}$ evolution in the $M_{\text{BH}} - M_{\text{DH}}$ relation, although large errors are such that we can not exclude the possibility of there being no evolution. We derive the zero-point of the $M_{\text{BH}} - M_{\text{DH}}$ relation (averaged over redshift) and find it to be $M_{\text{BH}} = 10^{8.4 \pm 0.2} M_{\odot}$ for a dark matter halo of mass $M_{\text{DH}} = 10^{12.5} M_{\odot}$. This is most consistent with a model using a Seljak (2004) dark matter profile (under the assumption of no evolution in $M_{\text{BH}} - M_{\text{DH}}$), however, uncertainties are such that we are unable to definitively distinguish which model is preferred. We compare our measured $M_{\text{BH}} - M_{\text{DH}}$ relation to that derived from hydrodynamical simulations of galaxy evolution (Di Matteo, Springel, & Hernquist 2005; Robertson et al. 2005) and find good agreement.

We note that because QSOs are selected above a given luminosity this will tend to select objects above a given M_{BH} . This results in a Malmquist-type bias such that the observed mean M_{BH} will lie above the true $M_{\text{BH}} - M_{\text{DH}}$ relation. The level of bias is crucially dependent on the amount of scatter in the $M_{\text{BH}} - M_{\text{DH}}$ relation.

We take a subsample of QSOs in a constant magnitude interval around $M_{b_J}^*$ and find significant evolution in their black hole masses characterised by $M_{\text{BH}} \propto (1+z)^{3.3 \pm 1.1}$. Comparing this to the observed lack of significant evolution

in Eddington ratio ($L/L_{\text{Edd}} \propto (1+z)^{-0.4 \pm 1.1}$) we conclude that luminosity evolution of L^* QSOs is driven primarily by decreasing black hole masses between redshifts 2.5 and 0.5. However, the exact combination of evolution in M_{BH} and L/L_{Edd} is dependent on the slope of the luminosity dependence in the virial mass estimator and any luminosity/redshift dependence in the velocity width of the QSO broad lines as well as the calibrations of the virial mass estimators themselves. Considering this and potential sources of systematic errors in our line width measurements, we find that our data are still consistent with a picture in which both reducing black hole masses and Eddington ratios play an equal role in L^* QSO luminosity evolution as observed in other studies (e.g. Merloni 2004; Heckman et al. 2004).

To extend this work further, detailed analysis of samples with a broader dynamic range will be required, including the analysis of QSO clustering as a function of luminosity. This has started to be done with small samples (e.g. Adelberger & Steidel 2005), but will be extended with new faint QSO surveys such as the 2dF-SDSS LRG and QSO (2SLAQ) Survey (Richards et al. 2005).

ACKNOWLEDGEMENTS

We warmly thank all the present and former staff of the Anglo-Australian Observatory for their work in building and operating both the 2dF and 6dF facilities. The 2QZ and 6QZ are based on observations made with the Anglo-Australian Telescope and the UK Schmidt Telescope. We would also like to thank all of the good people at the University of Sydney for their help, their advice and their on-going support.

REFERENCES

- Adelberger K.L., Steidel C.C., 2005, ApJ, 627, L1
 Barger A.J., Cowie L.L., Mushotzky R.F., Yang Y., Wang W.-H., Steffen A.T., Capak P., 2005, AJ, 129, 578
 Corbett E.A., Croom S.M., Boyle B.J., Netzer H., Miller L., Outram P.J., Shanks T., Smith R.J., Rhook K., 2003, MNRAS, 343, 705
 Cristiani S., Vio R., 1990, A&A, 227, 385
 Croom S.M., Boyle B.J., Shanks T., Smith R.J., Miller L., Outram P.J., Loaring N.S., Hoyle F., da Ângela J., 2005, MNRAS, 356, 415
 Croom S.M., Rhook K., Corbett E.A., Boyle B.J., Netzer H., Loaring N.S., Miller L., Outram P.J., Shanks T., Smith R.J., 2002, MNRAS, 337, 275
 Croom S.M., Smith R.J., Boyle B.J., Shanks T., Miller L., Outram, P.J., Loaring N.S., 2004, MNRAS, 349, 1397 (Paper XII)
 Di Matteo T., Springel V., Hernquist L., 2005, Natur, 433, 604
 Elvis M., et al., 1994, ApJs, 95, 1
 Ferrarese L., 2002, ApJ, 578, 90
 Ferrarese L., & Merritt D., 2000, Apj. Lett., 539, L9
 Francis P.J., Hewett P.C., Foltz C.B., Chaffee F.H., Weymann R.J., Morris S.L., 1991, ApJ, 373, 465
 Gebhardt K., Bender R., Bower G., Dressler A., Faber S.M., Filippenko A.V., Green R., Grillmair C., Ho L.C., Kormendy J., Lauer T.R., et al., 2000, Apj. Lett., 539, L13
 Heckman T.M., Kauffmann, G., Brinchmann J., Charlot S., Tremonti C., White S.D.M., ApJ, 613, 109
 Hopkins P.F., Hernquist L., Cox T.J., Robertson B., Springel V., 2006, ApJS, 163, 50
 Kaspi S., Maoz D., Netzer H., Peterson B.M., Vestergaard M., Jannuzi B.T., 2005, ApJ, 629, 61
 Kaspi S., Smith P.S., Netzer H., Maoz D., Jannuzi B.T., Giveon U., 2000, ApJ, 533, 631
 Kormendy J., Richstone D., 1995, Ann. Rev. Astron. Astrophys., 33, 581
 Marziani P., Sulentic J.W., Dultzin-Hacyan D., Calvani M., Moles M., 1996, ApJS, 104, 37
 Magorrian J., Tremaine S., Richstone D., Bender R., Bower G., Dressler Alan., Faber S.M., Gebhardt K., Green R., Grillmair C., Kormendy J., Lauer T., 1998 AJ, 115, 2285
 McLure R.J., Dunlop J.S., 2002, MNRAS, 331, 795
 McLure R.J., Dunlop J.S., 2004, MNRAS, 352, 1390
 McLure R.J., Jarvis M.J., 2002, MNRAS, 337, 109
 Merloni A., 2004, MNRAS, 353, 1035
 Miller L., Percival W.J., Croom S.M., 2005, [astro-ph/0506591]
 Mo H.J., White S.D.M., 1996, MNRAS, 282, 347
 Navarro J.F., Frenk C.S., White S.D.M., 1997, ApJ, 490, 493
 Percival W., et al., 2002, MNRAS, 337, 1068
 Peterson B.M., et al., 2004, ApJ, 613, 682
 Press W.H., Flannery B.P., Teukolsky S.A., Vetterling W.T., 1989, Numerical Recipes (Cambridge: Cambridge Univ. Press)
 Richards G.T. et al. 2005, MNRAS, 360, 839
 Richards G.T., et al. 2006, [astro-ph/0601558]
 Richards G.T., Vanden Berk D.E., Reichard T.A., Hall P.B., Schneider D.P., SubbaRao M., Thakar A.R., York D.G., 2002, AJ, 124, 1
 Robertson B., Hernquist L., Cox T.J., Di Matteo T., Hopkins P.F., Martini P., Springel V., 2006, ApJ, 641, 90
 Schlegel D.J., Finkbeiner D.P., Davis M., 1998, ApJ, 500, 525
 Seljak U., 2002, MNRAS, 334, 797
 Smith J.E., Young S., Robinson A., Corbett E.A., Giannuzzo M.E., Axon D.J., Hough J.H., 2002, MNRAS, 335, 773
 Spergel D. N., et al., 2003, ApJS, 148, 175
 Vanden Berk D.E., Richards G.T., Bauer A., Strauss M.A., Schneider D.P., Heckman T.M., York D.G., Hall P.B., Fan X., Knapp G.R., et al., 2001, AJ, 122, 549
 Vestergaard M., 2002, ApJ, 571, 733
 Vestergaard M., Peterson B.M., 2006, [astro-ph/0601303]
 Vestergaard M., Wilkes B.J., 2001, ApJS, 134, 1
 Wandel A., Peterson B.M., Malkan M.A., 1999, ApJ, 526, 579
 Wang T.G., Lu Y.J., Zhou Y.Y., 1998, ApJ, 493, 1
 Wills B.J., Netzer H., Brotherton M.S., Han M., Wills D., Baldwin J.A., Ferland G.J., Browne I.W.A., 1993, ApJ, 410, 534
 Wytthe J.S.B., Loeb A., 2005, ApJ, 621, 95